Nano-environment effects on the luminescence properties of Eu3+-doped nanocrystalline SnO2 thin films

Samad Bazargan and K. T. Leung

Citation: J. Chem. Phys. **137**, 184704 (2012); doi: 10.1063/1.4765099
View online: http://dx.doi.org/10.1063/1.4765099
View Table of Contents: http://jcp.aip.org/resource/1/JCPSA6/v137/i18
Published by the American Institute of Physics.

Nano-environment effects on the luminescence properties of Eu^{3+}-doped nanocrystalline SnO_2 thin films

Samad Bazargan and K. T. Leung[a)]
WATLab and Department of Chemistry, University of Waterloo, Waterloo, Ontario N2L 3G1, Canada

(Received 9 August 2012; accepted 11 October 2012; published online 12 November 2012)

Nanocrystalline tin (IV) oxide thin films doped with Eu^{3+} ions are synthesized using a simple spin-coating method followed by postannealing in an O_2 flow at 700 °C. Transmission electron microscopy and x-ray photoelectron spectroscopy studies illustrate the incorporation of Eu^{3+} ions in the films with a high atomic percentage of 2.7%–7.7%, which is found to be linearly dependent on the initial concentration of Eu^{3+} in the precursor solution. Glancing incidence x-ray diffraction results show that the crystalline grain sizes decrease with increasing the Eu^{3+} concentration and decreasing the postannealing temperature with the emergence of the $Eu_2Sn_2O_7$ phase at high Eu^{3+} concentrations (≥5.3 at.%). Luminescence spectra of these doped samples show the characteristic narrow-band magnetic dipole emission at 593 nm and electric dipole emission at 614 nm of the Eu^{3+} ions, arising from UV absorption at the SnO_2 band-edge followed by energy transfer to the emission centers. Manipulating the crystallite size, composition, and defect density of the samples greatly affects the absorption edge, energy transfer, and therefore the emission spectra. These modifications in the environment of the Eu^{3+} ions allow the emission to be tuned from pure orange characteristic Eu^{3+} emission to the broadband emission corresponding to the combination of strong characteristic Eu^{3+} emission with the intense defect emissions. © *2012 American Institute of Physics*. [http://dx.doi.org/10.1063/1.4765099]

I. INTRODUCTION

Tin (IV) oxide (TO) is a wide band gap semiconductor with numerous applications in chemical sensing,[1,2] transparent conducting electrodes for displays, thin-film transistors, solar cells, optoelectronics,[3] and catalysis.[4] Due to its wide energy band gap (3.6 eV), TO exhibits high transparency of ca. 90% in the visible region. Meanwhile, the abundance of point defects, e.g., anion deficiency and cation interstitial, in TO and other transparent conducting oxides (TCO), act as carrier generators in these oxides, resulting in their high levels of conductivity.[5] These defects have also been proposed to act as radiative recombination centers contributing to the photoluminescence properties of these oxides in the visible region, in addition to their band edge UV emission.[6] The emission peaks generated by these intrinsic defects in the bulk of TCO are, however, very broad, and there is little to no control on their peak emission wavelength. Inducing sharp photon emission lines in the luminescence spectrum of these oxides with control on their emission wavelength is of great interest to their potential application in photonics and optoelectronics, including the development of light emitting diodes and lasers, and phosphors for display using these stable, nontoxic and inexpensive oxides as the active materials.

In the past two decades, research in this field has attracted a growing interest due to the observed enhanced luminescence properties in nanostructured materials as a result of the quantum confinement effects[7] and/or the improved energy transfer from the host to the emission centers, e.g., defect sites, in these nanoscale structures.[8–10] However, studies on the intrinsic and surface defects of nanostructures have shown their effectiveness in the control of the luminescence only in a limited range of wavelengths, e.g., in the UV to blue region for most TCO nanoparticles.[8–10] Incorporation of appropriate external dopants in these nanostructures therefore represents a promising approach to tuning the luminescence spectrum throughout the visible region, where the dopant sites act as recombination centers and create strong luminescence as already observed for the Mn-doped ZnS nanoparticles.[11] Among the different possible dopants, rare earth ions including those of Eu, Tb, Er, Ce, Tm, Ho, and Nd are the most attractive because of their characteristic electronic transitions that could lead to sharp luminescence features in the UV to infrared range.[12,13] The Eu^{3+} ion is of particular interest due to two characteristic orange emissions at ~614 nm and 593 nm, which correspond to an electric dipole transition ($^5D_0$-$^7F_2$) and a magnetic dipole transition ($^5D_0$-$^7F_1$), respectively.[13] Depending on the symmetry of the occupancy site of Eu^{3+} ion in the lattice, one of these transitions will dominate because of the different nature of these transitions. Since an electric dipole transition is only allowed in a non-centrosymmetric crystal field, substitution in the symmetric sites will produce predominantly the 593 nm emission, while non-symmetric site occupancy will lead to a dominant 614 nm emission.[14] A variety of methods including sol-gel,[15–17] solid-state reaction[18] solvothermal,[19] and other solution-phase techniques[20–22] have been employed for doping rare earth ions (including Eu^{3+}) into the nanostructures of TO. Nanoparticles of TO with dopant concentrations of 1–5 at.% could be produced in the powder form or embedded in glass

a)Electronic mail: tong@uwaterloo.ca.

by using these methods. Future optoelectronic applications of these nanostructures can only be realized upon successful incorporation of these nanostructures into device structures as films. Enabling the control on the luminescence properties of TO films in combination with their transparency and conductivity could therefore have a great impact on the applications of these functional materials as transparent electronics components. However, assembly of nanoparticles in a film and the interfaces formed among the nanoparticles alter their properties from those of (individually separable) nanoparticles drastically. Therefore, it is important to investigate the effects of nanocrystallites and particularly such nano-environments on the energy transfer and luminescence properties of TO films.

Here, we present a systematic study of the effects of introducing Eu^{3+} dopants (up to a level as high as 20 mol.% in the precursor solution) into nanocrystalline TO film on their physical and compositional structures and on the luminescence properties of these conductive nanocrystalline films. We use a simple spin-coating method to dope Eu^{3+} ion into TO nanostructures. This synthesis method enables us to incorporate Eu^{3+} ions homogeneously into the initially amorphous TO matrix beyond the solubility limit of crystalline TO ($\sim$0.06 mol.%[23]) with concentrations as high as 20 mol.%, which is difficult to achieve using sol-gel and solvothermal methods reported for the similar studies. Annealing this Eu-doped matrix to the post-anneal temperature (T_{Anneal}) leads to nanocrystallite formation with controllable sizes that depend on the dopant concentration and T_{Anneal}. The nanocrystalline films so obtained exhibit an effective energy transfer from the TO host to Eu^{3+} ions upon photoexcitation. Intense photoluminescence peaks characteristic of the Eu^{3+} emission at 614 nm and 593 nm as well as defect-related emission peaks below 550 nm are observed for the homogeneously doped TO nanostructures. The interplay between the TO nanocrystallites and the amorphous matrix/impurity phase leads to variation in the relative intensities of these peaks, which could be manipulated by changing the dopant concentration and T_{Anneal}. Our result shows that it is possible to obtain either a pure characteristic Eu^{3+} emission or a broadband emission containing both Eu bands and defect-related bands for the same (10 mol.%) Eu-doped film by controlling T_{Anneal} (700 °C for the former and 500 °C for the latter).

II. EXPERIMENTAL DETAILS

The method that we use to obtain a nanocrystalline TO film has been described in our recent work.[24] Briefly, a clear precursor solution is prepared by dissolving $SnCl_4 \cdot 5H_2O$ salt (98% purity, Aldrich), mixed with an appropriate amount of $Eu(NO_3)_3 \cdot 5H_2O$ salt (99.9% purity, Aldrich), in isopropanol by vigorous stirring for at least 2 h. In particular, starting with a 2 M concentration of the tin salt in isopropanol, we add appropriate amounts of $Eu(NO_3)_3 \cdot 5H_2O$ to obtain the molar percentages of 0%, 2%, 5%, 10%, and 20%, the resulting TO films of which will be referred to as SnO_2, Eu 2%, Eu 5%, Eu 10%, and Eu 20%, respectively, in the present work. The precursor solutions are then spin-coated on chemically oxidized Si(100) substrates followed by post-annealing for 90 min at 700 °C in a flowing O_2 atmosphere (at a flow rate of $\geq$70 sccm). Two separate Eu 10% films with T_{Anneal} of 500 °C and 900 °C are also prepared in order to study the effect of annealing temperature on the photoluminescent emission through suppressing or promoting the film crystallization. The present procedure allows us to produce TO films with uniform morphology and a film thickness of 150 $\pm$ 25 nm.

Surface morphology of the resulting films is studied by scanning electron microscopy (SEM) in a LEO 1530 FE-SEM microscope. Their crystalline structures are characterized by glancing-incidence x-ray diffraction (GIXRD) in a PANalytical MRD X'pert Pro diffractometer at an incidence angle of 0.3°, while the local crystalline structure and composition of the nanocrystallites are examined by transmission electron microscopy (TEM) in a FEI Tecnai F20 operated at 200 kV. Chemical-state compositions of the samples are analysed by x-ray photoelectron spectroscopy (XPS) in a Thermo-VG Scientific ESCALab 250 Microprobe with a monochromatic Al Kα source (1486.6 eV). Reflectance spectra of the samples are recorded by using a Perkin-Elmer Lambda 35 UV-Vis spectrometer equipped with a Labsphere integrating sphere, and the photoexcitation and emission spectra of the samples are collected by using a Perkin-Elmer LS-55 fluorescence spectrometer equipped with a Xe lamp excitation source.

III. RESULTS AND DISCUSSION

A. Morphology and crystal structure of Eu-doped films

Figure 1 compares the SEM image of the SnO_2 film with those obtained with different Eu concentrations (Eu 5%, Eu 10%, and Eu 20%), all with post-annealing at 700 °C, and with those of the Eu 10% samples obtained with post-annealing at 500 °C and 900 °C. It should be noted that all the films remain highly conductive as illustrated by their

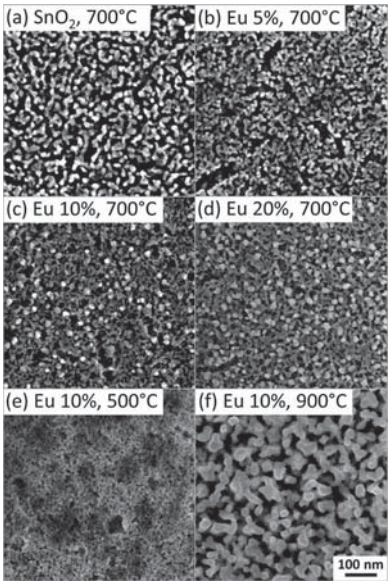

FIG. 1. SEM images of (a) SnO_2 film (without Eu doping) and (b) Eu 5%, (c) Eu 10%, and (d) Eu 20% films, all obtained with T_{Anneal} = 700 °C, and SEM images of the Eu 10% films obtained with T_{Anneal} of (e) 500 °C, and (f) 900 °C.

respective SEM images obtained without any conductive layer coating. Evidently, the SnO_2 film exhibits a granular structure with a grain size of 10–20 nm (Figure 1(a)). The Eu 2% film (not shown) and the Eu 5% film (Figure 1(b)) are found to have similar granularity, where the grains are less prominent and they tend to fuse into one another. For the Eu 10% (Figure 1(c)) and Eu 20% films (Figure 1(d)), a web-like structure is formed with some distinctly brighter grains (10–20 nm in size) on top of this layer. The presence of these grains suggests the formation of a new phase in these highly doped films. The Eu 10% films prepared with T_{Anneal} = 500 °C (Figure 1(e)) and 900 °C (Figure 1(f)) show a significantly different morphology than that prepared with T_{Anneal} = 700 °C (Figure 1(c)). The Eu 10% film obtained with T_{Anneal} = 500 °C shows a porous film-like morphology without any discernible grains (Figure 1(e)), while the Eu 10% film prepared with T_{Anneal} = 900 °C exhibits a distinct granular morphology (Figure 1(f)) with the grains more separated and considerably larger (20–30 nm in size) than those observed in any of the films obtained with T_{Anneal} = 700 °C (Figure 1(c)). These observations suggest that the Eu 10% film prepared with T_{Anneal} = 500 °C is mainly amorphous, and crystallization has not occurred due to insufficient thermal energy. On the other hand, the Eu 10% film prepared with T_{Anneal} = 900 °C is highly crystalline with homogeneous crystallization over the entire film, unlike that observed for the Eu 10% sample obtained with T_{Anneal} = 700 °C.

In order to investigate the effect of Eu doping on the crystalline structure of the nanocrystalline TO film, we perform GIXRD on all the samples (Figure 2). The GIXRD pattern for the SnO_2 film shows a single polycrystalline tetragonal SnO_2 phase (PDF2#00-041-1445), and the Debye-Scherrer analysis performed on the most prominent (110) peak at 26.62° (by assuming peak broadening due only to a size effect) gives a crystallite size of 8 nm. Upon doping, the intensities of all the peaks for the Eu 2% and Eu 5% samples are found to greatly reduce, suggesting that the presence of Eu ions is suppressing the crystallization of the TO film, which is also consistent

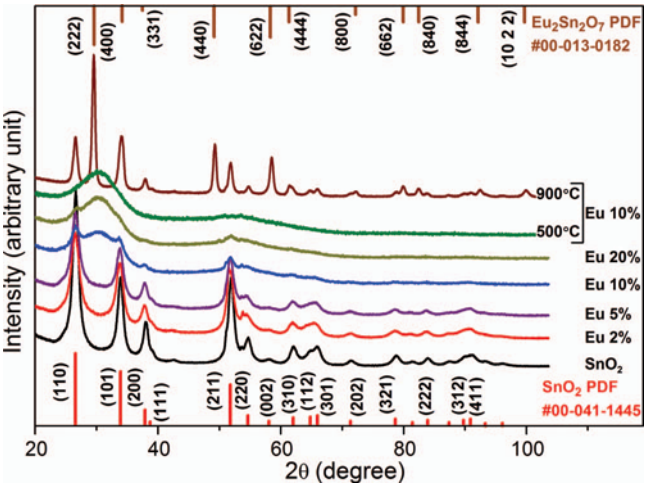

FIG. 2. Glancing-incidence XRD patterns of the SnO_2 and Eu-doped films (Eu 2%, Eu 5%, Eu 10%, and Eu 20%), all obtained with post-annealing at 700 °C, and of the Eu 10% films obtained with post-annealing at 500 °C and 900 °C.

with the smaller estimated crystallite sizes (5 nm) than that of the undoped SnO_2 sample. Their corresponding (110) peak positions are also shifted to a smaller angle by 0.08° for Eu 2% and by 0.05° for Eu 5%, which indicates an increase in the lattice constant of the TO nanocrystallites by 0.3%–0.2%, likely as a result of the substitution of Sn^{4+} ion (with an ionic radius of ~0.71 Å[13]) by the bigger Eu^{3+} ion (~0.98 Å[13]) in the host lattice. For the Eu 10% or Eu 20% film, their crystallinity appears to be greatly suppressed, with the emergence of an intense broad peak near 30° and a weaker broad peak at 53°, while the (110), (101), and (211) TO peaks becoming barely detectable. The GIXRD pattern for the Eu 10% film prepared with T_{Anneal} = 500 °C is found to be similar to that of the Eu 20% film obtained with T_{Anneal} = 700 °C, with only the broad peaks at 30° and 53° remaining, and total disappearance of the TO crystalline peaks. According to the Scherrer analysis, the large FWHM (6.68°) of the feature at 30° corresponds to crystallites with an average size of ~1 nm, i.e., poor crystallinity. On the other hand, the GIXRD pattern for the Eu 10% obtained with T_{Anneal} = 900 °C reveals a new cubic pyrochlore $Eu_2Sn_2O_7$ phase (PDF2#00-013-0182), in addition to the tetragonal SnO_2 phase. The appearance of the most intense (222) peak of the $Eu_2Sn_2O_7$ phase at 29.56° suggests that the broad peak at ~30° found for the Eu 10% and Eu 20% films could be due to the emergence of this phase. The GIXRD results therefore show that Eu doping is suppressing the growth of TO nanocrystallites to bigger sizes, leading to the formation of a poorly crystalline $Eu_2Sn_2O_7$ phase. This TO crystallization can also be greatly inhibited by decreasing T_{Anneal} to 500 °C. Increasing T_{Anneal} to 900 °C, however, leads to crystallization of both SnO_2 and $Eu_2Sn_2O_7$ phases with larger crystallite sizes (of 12 nm and 15 nm, respectively) than the samples prepared with T_{Anneal} = 700 °C, consistent with the SEM results (Figure 1).

To further investigate the nature of crystallinity of the nanocrystallites and the homogeneity of the Eu doping in these TO films, we conduct TEM studies on selected Eu-doped TO films. The scanning TEM image of a thin cross section of the Eu 2% film obtained with T_{Anneal} = 700 °C, prepared by focused ion beam microscopy (Figure 3(a)), clearly shows the formation of TO nanocrystalline grains with an average size of 10 nm, which are present in the entire ~150 nm thickness of the film. Closer examination of the voids inside the film shows an amorphous phase surrounding the nanocrystallites (Figure 3(a), inset). The appearance of this amorphous matrix connecting the grains is consistent with the observation of fused grain morphology in the SEM images (Figure 1). Energy dispersive x-ray (EDX) analysis further reveals the presence of SiO_x layer on the chemically oxidized Si substrate. More importantly, EDX maps for the Sn, O, and Eu elements (Figure 3(b)) indicate a homogeneous distribution of the Eu ions over the entire thickness of the TO film.

Figure 4(a) shows the high-resolution TEM image of a thin cross section of the Eu 10% film obtained with T_{Anneal} = 700 °C (prepared by focused ion beam microscopy). In addition to the TO nanocrystallites (Figure 4(a), circle), other nanocrystallites of smaller sizes (~3 nm) (Figure 4(a), oval) with a crystalline structure close to $Eu_2Sn_2O_7$ are also observed. The observed lattice spacing in this $Eu_2Sn_2O_7$

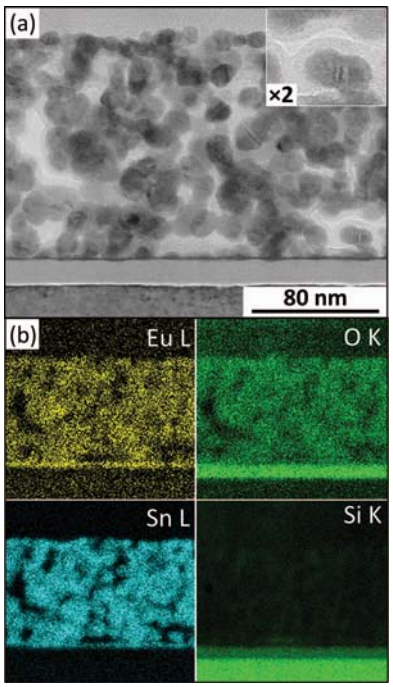

FIG. 3. (a) Scanning TEM image, and (b) energy dispersive x-ray maps of Eu L, Sn L, O K, and Si K lines of a thin cross section of the Eu 2% film obtained with $T_{Anneal} = 700\,^{\circ}C$, prepared by focused ion beam microscopy. Inset shows a magnified view of nanocrystallites surrounded by an amorphous layer.

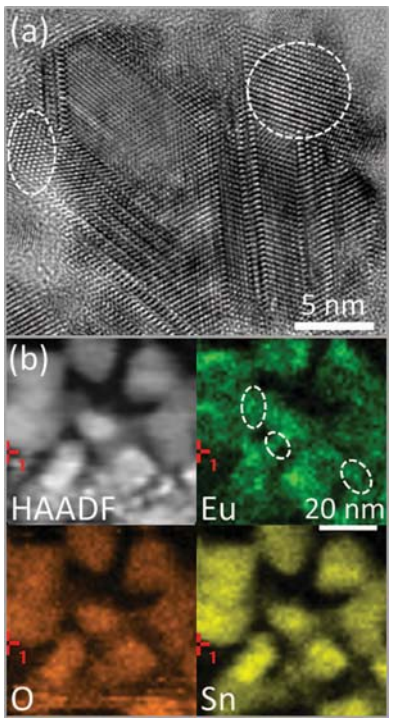

FIG. 4. (a) High-resolution TEM image and (b) high angle annular dark field (HAADF) image and the corresponding energy dispersive x-ray maps of Eu L, Sn L, O K lines of a thin cross section of the Eu 10% film obtained with $T_{Anneal} = 700\,^{\circ}C$ (prepared by focused ion beam microscopy). The circle and oval in (a) mark a SnO_2 and a $Eu_2Sn_2O_7$ nanocrystallites, respectively, and the ovals in (b) mark the presence of Eu between the Sn-rich grains.

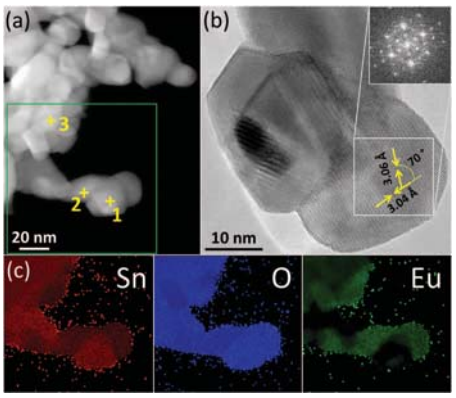

FIG. 5. (a) Dark-field TEM image of the nanocrystallites scraped off from a Eu 10% film obtained with $T_{Anneal} = 900\,^{\circ}C$, and (c) the corresponding EDX maps of Sn L, O K, and Eu L lines over the region marked by the green box (inset) in (a), and (b) high-resolution TEM image of selected grains studied in the EDX mapping with the inset showing the Fourier transform of the box marked in (b). Crosses in inset in (a) mark the EDX point quantification locations for the (1) Eu-deprived, (2) Eu-rich, and (3) stacked grain regions.

nanocrystallite is found to be 5.4 Å, in close agreement with the (111) interplane spacing (6.0 Å) for the reference pattern (PDF2#00-013-0182) given the poor crystallinity as observed in our GIXRD study (Figure 2). In particular, the observed minor difference could be due to distortions in the crystal structure as a result of stress exerted from the amorphous phase and/or of the small size of the nanocrystallites. Moreover, the corresponding EDX maps for the Sn, O, and Eu elements (Figure 4(b)) also confirm that Eu is dispersed homogeneously inside the TO grains. Furthermore, the Eu signal is found to extend in the small areas (marked by ovals in Figure 4(b)) among the grains with a strong Sn signal, indicating the formation of a new phase with a relatively higher Eu concentration. This new phase could be assigned to $Eu_2Sn_2O_7$, as is observed in the smaller nanocrystallites in the high-resolution TEM image (Figure 4(a), marked by oval).

Figure 5 shows the TEM image of the Eu 10% film prepared with $T_{Anneal} = 900\,^{\circ}C$, depicting the formation of considerably larger grains (20–25 nm) compared to those observed for the Eu 2% film (10 nm, Figure 3), in good accord with the GIXRD results (Figure 2). The corresponding EDX maps (Figure 5(c)) clearly reveal the phase separation between the Eu-deprived grains containing only Sn and O (marked as region 1, Figure 5(a), inset) and the Eu-rich grains containing Sn and O, as well as Eu (marked as region 2, Figure 5(a), inset). Quantification results show 32 at.% Sn and 68 at.% O for region 1, and 20 at.% Eu, 20 at.% Sn, and 60 at.% O for region 2, which confirms the respective stoichiometries of the SnO_2 and $Eu_2Sn_2O_7$ phases. Performing quantification on a stack of crystallites (region 3, Figure 5(a), inset) shows 5 at.% Eu, 28 at.% Sn, and 66 at.% O. This corresponds to a Eu-to-Sn mole ratio of 0.18, which is in fair accord with that (0.10) for the 10% dopant concentration used for the precursor solution, especially considering the limited sampling size of a few grains. The high-resolution TEM image (Figure 5(b)) shows the atomic columns inside an Eu-rich crystallite with two sets of lattice spacings of 3.04 Å and 3.06 Å making a 70° angle, which can also

be shown in the corresponding Fourier-transform pattern (Figure 5(b), inset). These observations are in good agreement with the cubic structure and the 3.01 Å lattice spacing of the (222) planes in the bulk $Eu_2Sn_2O_7$ phase (PDF2#00-013-0182). These results therefore definitively show that post-annealing at high T_{Anneal} (900 °C) facilitates the formation of phase-segregated nanocrystallites (20–25 nm) of SnO_2 and $Eu_2Sn_2O_7$.

In summary, our TEM studies show that Eu is homogeneously incorporated into the TO structure for Eu dopant concentration below 10% and $T_{Anneal} = 700$ °C. Increasing the Eu dopant concentration leads to the formation of a $Eu_2Sn_2O_7$ phase with small crystallite sizes (~3 nm). Phase separation of the $Eu_2Sn_2O_7$ phase from the SnO_2 phase is facilitated by increasing T_{Anneal} to 900 °C, which leads to the formation of 20–25 nm nanocrystallites of SnO_2 and $Eu_2Sn_2O_7$.

B. Chemical-state composition

In order to investigate the chemical-state compositions and the dopant homogeneity over the film thickness of the doped TO films, we perform a comprehensive depth-profiling XPS study on the samples. Figure 6 shows typical XPS results for the Eu 2% film. The survey spectrum (Figure 6(a)) depicts that all the observed peaks can be attributed to Sn, O and Eu, with no detectable impurity residual from the precursor solution. It should be noted that the minor carbonaceous layer observed on the as-prepared film due to sample handling in ambient conditions can be easily removed after light Ar sputtering for 60 s. The Sn $3d_{5/2}$ peak at 487.4 eV for the as-prepared film is found to be shifted after the light sputtering and remains unchanged at 487.0 eV upon further sputtering (Figure 6(e)). The peak at 487.0 eV can be attributed to the Sn^{4+} state, in good accord with our earlier study and the reference spectra for SnO and SnO_2 powders.[24] The corresponding O 1*s* (Figure 6(d)) and Eu $3d_{5/2}$ peaks (Figure 6(c)) also exhibit a similar shift in the peak position after the first sputtering step, which can also be explained by the removal of the carbonaceous layer. The O 1*s* peak for the as-prepared film is found to have two components with the intense peak at 531.3 eV and a weaker component at 532.9 eV. The higher binding energy component, which is observed for the undoped SnO_2 sample, has also been found in our previous study[24] and can be attributed to "chemisorbed oxygen" species on the surface of TO.[25] After the first sputtering step (of 60 s), the O 1*s* peak is found to be at 530.9 eV, without any evidence of the higher binding energy component (Figure 6(d)), confirming the surface-related nature of this component. Further sputtering for 240 s and 600 s does not affect the position and shape of the O 1*s* peak, indicating a homogeneous oxide layer throughout the film (before reaching the Si interface).

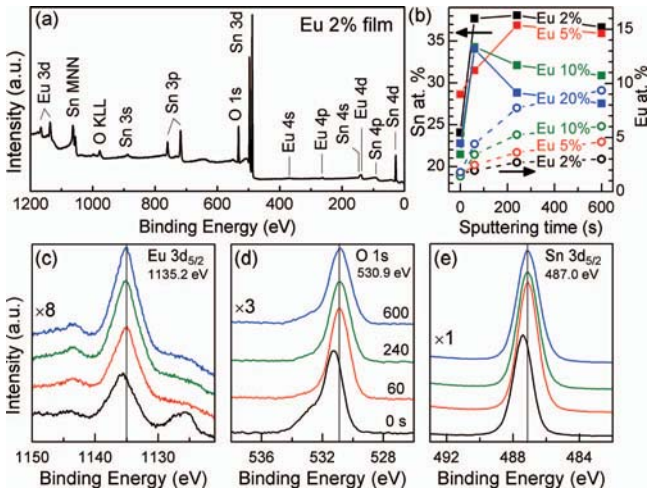

FIG. 6. (a) Survey XPS spectrum after 240 s Ar sputtering, and XPS spectra of (c) Eu $3d_{5/2}$, (d) O 1*s*, and (e) Sn $3d_{5/2}$ regions for the Eu 2% film without and with 60 s, 240 s, and 600 s of Ar sputtering. (b) Depth profiles of Sn $3d_{5/2}$ (solid lines) and Eu $4d_{5/2}$ (dashed lines) for Eu 2%, Eu 5%, Eu 10%, and Eu 20% films obtained with $T_{Anneal} = 700$ °C.

The XPS spectrum of Eu 3*d* region is complicated due to the possible valence fluctuations between the 2+ and 3+ oxidation states[26] and the resulting shake-down and shake-up satellite peaks.[27,28] For the as-prepared Eu 2% film, the intense Eu $3d_{5/2}$ peak at 1135.6 eV is observed along with a much weaker shake-up peak at 1144.3 eV[29] that persists upon sputtering. The lower binding energy Eu $3d_{5/2}$ peak at 1125.6 eV is only observed for the as-prepared film and is removed after sputtering for 60 s, suggesting a surface-related feature. This peak is assigned to the Eu^{2+} state, as is reported in earlier XPS studies of trivalent compounds of Eu.[27,28] The presence of this 2+ state has been proposed to be the result of a spontaneous surface valence transition from the Eu^{3+} state due to change in the local density of states at the surface.[27,28] In the present work, however, we only observe this Eu^{2+} state for the as-prepared Eu 2% film, which is therefore likely not a final-state effect but a surface-related shake-down transition. This is of great importance for the luminescence properties of Eu ions as the 2+ ion does not show luminescence properties, and reduction of the initial Eu 3+ ion to 2+ ion could have reduced the effective luminescence of the films. Upon further sputtering, the intensities of the Eu $3d_{5/2}$ peaks at 1135.2 and 1144.3 eV are found to increase with increasing sputtering time, in contrast to that observed for Sn $3d_{5/2}$ and O 1*s* features. This could likely be due to a lower preferential sputtering rate for the heavier Eu element than those of the lighter Sn and O elements.

The XPS spectra of Sn $3d_{5/2}$, O 1*s*, and Eu $3d_{5/2}$ regions for the other Eu-doped samples prepared with $T_{Anneal} = 700$ °C and 900 °C are found to be similar to those of Eu 2% sample for both the as-prepared film and upon Ar sputtering. The relative intensities of the peaks are found to be different for different Eu-doped samples which will be discussed below. Using the fitted peak area as relative intensities and applying the appropriate relative sensitivity factors for Eu $4d_{5/2}$ (2.488), Sn $3d_{5/2}$ (4.725), and O 1*s* (0.711),[29] we estimate the relative chemical-state composition of Eu $4d_{5/2}$ for the four Eu-doped films prepared with $T_{Anneal} = 700$ °C for different sputtering steps. Because only the Eu $4d_{5/2}$ relative sensitivity factor is available, we estimate the corresponding Eu $4d_{5/2}$ intensity by applying an area ratio between the Eu $4d_{5/2}$ and Eu $3d_{5/2}$ peaks (1.45/1.84) to our fitted area for the Eu $3d_{5/2}$ peak (Figure 6(a)). Figure 6(b) shows the resulting depth profiles of Eu $4d_{5/2}$ and Sn $3d_{5/2}$ for all the Eu-doped films. Evidently,

both the Eu $4d_{5/2}$ and Sn $3d_{5/2}$ profiles exhibit a sharp rise after 60 s and a plateau after 240 s of sputtering, as observed in our earlier work. This "plateau" value may be used as a relative indicator of the actual dopant level of Eu in the TO film. Furthermore, the "plateau" values are found to be 2.7%, 3.6%, 5.3%, and 7.7% for the Eu 2%, Eu 5%, Eu 10%, and Eu 20% samples, respectively, which shows a linear relation ($R^2 = 0.9936$, slope = 0.28) to the initial 2-to-20% concentration of Eu in the precursor solution. The latter relation therefore allows us to have a better control of the actual dopant level based on the Eu initial concentration. The obtained dopant levels for Eu in combination with the corresponding concentration of Sn (38.1%, 36.9%, 32.1%, and 28.8%) yield Eu-to-Sn ratios of 0.07, 0.10, 0.16, and 0.27 for the Eu 2%, Eu 5%, Eu 10%, and Eu 20% films, respectively. It is noteworthy that the 0.16 ratio for Eu 10% sample is in good agreement with the 0.18 value obtained by using the EDX analysis above.

C. Optical properties

The photoluminescence (PL) emission spectra of the Eu-doped SnO_2 films (Figure 7) exhibit two sets of features, including a broad emission band below 550 nm decorated with a number of peaks at 529 nm, 485 nm, 460 nm, 448 nm, and 422 nm, and a set (above 550 nm) consisting of two bands at 593 nm and 614 nm. By comparing these spectra with that of the SnO_2 film (i.e., without any Eu doping, Figure 7), which exhibits only a broad emission with weak peaks at 529 nm, 485 nm, 448 nm, and 422 nm, we assign the first set of features, except for the 460 nm peak, of the Eu-doped TO films to the nanocrystalline TO phase. The feature at 460 nm and the second set of peaks at 593 nm and 614 nm are only observed for Eu-doped films and are characteristic $^5D_2$-$^7F_0$, $^5D_0$-$^7F_1$, and $^5D_0$-$^7F_2$ emission bands of the Eu^{3+} ions, respectively.[13,14,30] Interestingly, the intensities of the sharp peaks and the broad emission features associated with the TO phase differ significantly for different dopant concentrations, and for the Eu 10% films obtained with different post-annealing temperatures (Figure 7). In particular, the four sharp peaks observed below 550 nm corresponding to the nanocrystalline TO phase appear to be more intense for Eu 2% and Eu 5% films than those of SnO_2 film and they are very weak for the Eu 10% films obtained with $T_{Anneal} = 700\,^\circ C$ and 900 °C. Remarkably, their intensities are greatly increased for the Eu 20% film and for the Eu 10% film obtained with $T_{Anneal} = 500\,^\circ C$ (note the 1/40 change in scale for the latter in Figure 7). These results suggest that these four sharp nanocrystalline TO peaks below 550 nm are related to defect centers in the structure, which are expected to increase with increasing Eu concentration and with reducing post-annealing temperature. For the Eu 10% film obtained with $T_{Anneal} = 700\,^\circ C$, the intensities of these four peaks are however significantly reduced, which can be attributed to the formation of the new Eu-rich phase in this film (Figure 2) and its effects on radiative defect centers in the structure.

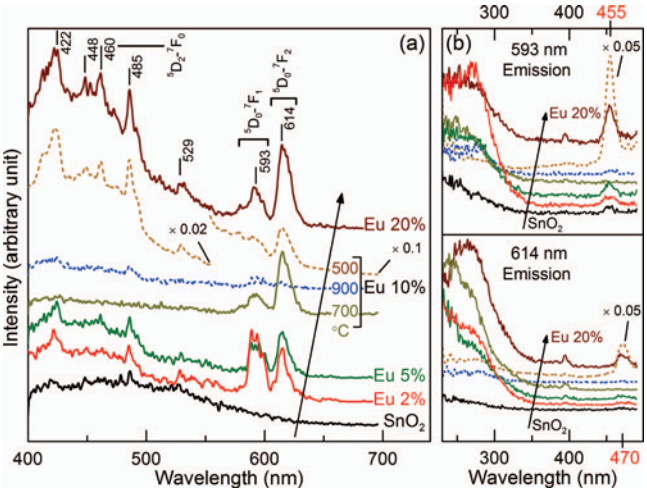

FIG. 7. (a) Photoluminescence emission spectra of the pristine and Eu-doped SnO_2 samples obtained with excitation wavelength of 300 nm. (b) The excitation spectra of the samples (with the same sequence as of the emission spectra shown by the arrows) for emission wavelengths of 614 nm (bottom) and 593 nm (top), corresponding to the magnetic dipole ($^5D_0$-$^7F_1$) and electric dipole ($^5D_0$-$^7F_2$) transitions of Eu^{3+} ions, respectively.

In general, the appearance and relative intensities of the two characteristic peaks of Eu reflect the symmetry of the lattice sites occupied by the Eu ions in the TO structure.[13,14,30] For the Eu 2% film, the 593 nm band is stronger than the 614 nm band, indicating that the majority of the Eu^{3+} ions occupy lattice sites with inversion symmetry, which correspond to the cationic site with C_{2h} symmetry of the TO structure (and not to, e.g., interstitial sites). On the other hand, for the Eu 5%, Eu 10%, and Eu 20% films obtained with $T_{Anneal} = 700\,^\circ C$, the 614 nm band is stronger than the 593 nm band, indicating that Eu^{3+} ions are mainly occupying substitutional sites with no inversion symmetry. These non-centrosymmetric centers could be found in interstitial sites and/or in the amorphous phase, or could be due to disturbance of the symmetric cationic sites with increase in the defect density. These defects are due to substitution of the bigger trivalent Eu^{3+} ion instead of the quadravalent Sn^{4+} ion, which causes distortions in the lattice structure and formation of oxygen vacancies.[13] The Eu 10% film obtained with $T_{Anneal} = 500\,^\circ C$ also shows a strong 614 nm band with a higher intensity than all the other films (note the 1/10 scaling factor), while the Eu 10% film obtained with $T_{Anneal} = 900\,^\circ C$ exhibits much weaker Eu emission peaks, with the 593 nm band stronger than the 614 nm band. This intensity variation shows that the amorphous structure in the former film promotes luminescence of Eu ions while the $Eu_2Sn_2O_7$ nanocrystallites in the latter film greatly suppress Eu emission.

We also collect the corresponding excitation spectra for the characteristic Eu^{3+} emission bands at 593 nm and 614 nm for all the films. These excitation spectra shown in Figure 7(b) exhibit a strong broad band below 330 nm in the UV region for all the films, which could be attributed to the optical absorption of the TO phase,[15,31] in good accord with the absorption edge observed between 3.9 eV (317 nm) and 3.7 eV (335 nm) for 4–12 nm pristine TO nanocrystallites.[32] Moreover, the intensity of this broad band appears to increase with increasing Eu concentration and decreasing T_{Anneal}, indicating that the energy transfer from TO structure to Eu is enhanced by the corresponding decrease in the nanocrystallite sizes and increase in the population of Eu emission centers

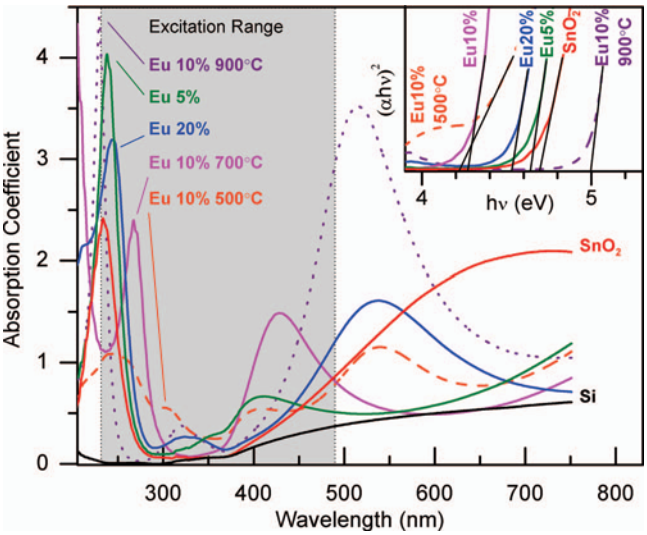

FIG. 8. Absorption coefficients of the samples obtained from their corresponding reflectance spectra using the Kubelka-Munk relation. Gray area marks the spectral range used for obtaining the excitation spectrum of samples for 614 nm and 593 nm emission lines in Figure 7(b). Inset illustrates the graphical extrapolating method used for obtaining the band gaps of the pristine and Eu-doped samples.

and density of defects in the TO structure. For the Eu 20% film obtained with $T_{anneal} = 700\,^{\circ}C$ and the Eu 10% film obtained with $T_{Anneal} = 500\,^{\circ}C$ (Figure 7(b)), we also observe an additional strong peak at 470 nm and 455 nm for the emission bands at 614 and 593 nm, respectively. These sharp peaks at 470 nm and 455 nm are assigned to direct excitation of the f–f transitions in Eu^{3+} ions, and although they are weak, they can also be detected for the low concentrations of Eu doping, e.g., the 455 nm line for the 593 nm emission band.[15,33] The nearly constant and featureless excitation spectra of Eu 10% film obtained with $T_{Anneal} = 900\,^{\circ}C$ suggests that the energy transfer from TO to Eu^{3+} is disrupted due to the phase separation and the Eu^{3+} in the large $Eu_2Sn_2O_7$ nanocrystallites does not exhibit any fluorescence properties.

Figure 8 shows the absorption spectra of the samples, which are converted from the respective reflectance spectra using the Kubelka-Munk relation: $\alpha = \frac{(1-R)^2}{2R}$, where α is the absorption coefficient and R is the reflectance.[34] Evidently, the Eu-doped samples exhibit extra peaks in the visible range of the spectra, and the doping concentration appears to affect their peak positions, likely due to the change in the crystallite size and phase of the samples. The gray area in Figure 8 marks the spectral region used for obtaining the excitation spectra of the samples shown in Figure 7(b). The increase in the intensity of the excitation spectra below 350 nm (Figure 7(b)) shows that absorption near the energy band-edge of TO (Figure 8) is responsible for the excitation of Eu^{3+} ions. Interestingly, band-edge absorption of all the Eu-doped samples are redshifted with respect to pure TO except for the Eu 10% samples obtained with $T_{Anneal} = 700\,^{\circ}C$ and $900\,^{\circ}C$. For the Eu 10% sample obtained with $T_{Anneal} = 700\,^{\circ}C$, the Eu-related absorption peak (at 267 nm) is blueshifted to fall in the excitation spectra range (Figure 8, gray box). Band gap (E_g) energy for TO (a direct band gap material) can be obtained by using the Tauc equation: $\alpha h\nu = A(h\nu - E_g)^{1/2}$, where A is a constant and $h\nu$ is the incident photon energy. Inset of Figure 8 shows the graphical method of determining the band gap by extrapolating the tangent of the curve near the absorption edge. The band gaps so obtained are 4.70 eV for pure TO, 4.64 eV for Eu 5%, and 4.53 eV for Eu 20% (all obtained with $T_{Anneal} = 700\,^{\circ}C$). Although the band gap of the Eu 10% sample obtained with $T_{Anneal} = 700\,^{\circ}C$, as defined by the most intense absorption peak, is 5.29 eV (not shown in inset), its band-edge absorption in the excitation range (gray box), originating from the blueshifted Eu-related peak, is 4.27 eV, and the corresponding band gaps for Eu 10% samples with $T_{Anneal} = 500\,^{\circ}C$ and $900\,^{\circ}C$ are found to be 4.22 eV and 5.00 eV, respectively.

The luminescence and absorption spectra reveal that emission for all of the doped samples, except for the Eu 10% sample obtained with $T_{Anneal} = 700\,^{\circ}C$, occurs by UV absorption at the TO band-edge, followed by energy transfer and finally emission at the Eu^{3+} ion sites. This energy transfer from the TO structure to Eu^{3+} is observed to be greatly affected by two correlated factors: the size of the nanocrystallites and the defect density. Decreasing the size of the nanocrystallites, i.e., increasing the defect density, improves the energy transfer from the TO structure to Eu^{3+} and increases the 614 nm emission intensity. This increase in the emission intensity at 614 nm is also accompanied with an increase in the defect-related emissions below 550 nm, which are found to be remarkably strong for Eu 20% film obtained with $T_{Anneal} = 700\,^{\circ}C$ and Eu 10% film obtained with $T_{Anneal} = 500\,^{\circ}C$. These defect-related emissions are, however, quenched for the Eu 10% film obtained with $T_{Anneal} = 700\,^{\circ}C$, where the nanocrystalline $Eu_2Sn_2O_7$ phase emerges, and the excitation occurs predominantly through UV absorption at the Eu-related absorption edge instead of the TO band gap absorption. These results show that by changing the Eu concentration and tuning T_{Anneal}, the emission spectra of the samples can be significantly modified. Among all these samples, the Eu 10% films obtained with $T_{Anneal} = 700\,^{\circ}C$ and $500\,^{\circ}C$ are of special interest, because the former has an intense pure Eu^{3+}-characteristic emission band at 614 nm, and the latter has the most intense emissions for both Eu^{3+}-characteristic band and defect-related bands below 550 nm.

IV. CONCLUSIONS

Uniform nanocrystalline TO films doped homogeneously with Eu^{3+} ions at 2.7–7.7 at.%, as determined from XPS results, have been prepared with a simple spin-coating method. The incorporation of Eu^{3+} ions in the TO structure is found to suppress the growth of the nanocrystallites, which leads to decrease in the crystallite sizes and formation of amorphous TO phase for the low doping levels (as observed for the Eu 2% and Eu 5% films) and to formation of a nanocrystalline $Eu_2Sn_2O_7$ phase for the high doping levels (as found for the Eu 10% and Eu 20% films). The characteristic Eu^{3+} emission bands centered on 593 nm and 614 nm are observed in these doped samples upon UV excitation. The majority of Eu^{3+} ions are found to occupy centrosymmetric cationic substitutional sites for the Eu 2% sample leading to an intense 593 nm emission, while for the Eu 5%, Eu 10%, and Eu 20% samples,

non-symmetric site occupation dominates with emission at 614 nm. These emissions occur by absorption at the TO band-edge followed by energy transfer to the Eu^{3+} ions, as shown in our excitation spectra. Incorporation of Eu^{3+} into the TO thin film structure and its effect on the nanocrystalline size and on the formation of defects and the new $Eu_2Sn_2O_7$ phase change the absorption band-edge of the films, which strongly affects the emission spectra of the samples. Increasing the Eu^{3+} concentration generally leads to an increase in the 614 nm emission intensity with respect to the 593 nm band and to an increase in the defect-related emission below 550 nm. However, in the case of the Eu 10% film obtained with $T_{Anneal} = 700\,^{\circ}C$, a pure Eu^{3+}-characteristic emission is observed, while the defect-related emissions appear to be all quenched likely due to the structural transformation and the emergence of $Eu_2Sn_2O_7$ phase. On the other hand, the Eu 10% film obtained with $T_{Anneal} = 500\,^{\circ}C$ has the strongest emission in both the Eu^{3+}-characteristic emission and the defect-related band below 550 nm resulting in a broadband emission. These results therefore illustrate that the nanocrystalline structure, defect density, and composition of the TO films can be used to modify the band structure, charge transfer efficiency, and defect versus Eu^{3+} emission probability, and therefore to control the luminescence properties of Eu-doped nanocrystalline TO films especially at high levels of Eu doping.

ACKNOWLEDGMENTS

The present work was supported by the Natural Sciences and Engineering Research Council of Canada.

[1]R. Dolbec and M. A. El Khakani, Appl. Phys. Lett. **90**, 173114 (2007).
[2]Y. Cheng, P. Xiong, C. S. Yun, G. F. Strouse, J. P. Zheng, R. S. Yang, and Z. L. Wang, Nano Lett. **8**, 4179–4184 (2008).
[3]T. Minami, Semicond. Sci. Technol. **20**, S35–S44 (2005).
[4]P. G. Harrison, *Chemistry of Tin* (Blackie, Glasgow, 1989).
[5]Ç. Kılıç and A. Zunger, Phys. Rev. Lett. **88**, 095501 (2002).
[6]S. Zhang, S.-H. Wei, and A. Zunger, Phys. Rev. B **63**, 1–7 (2001).
[7]M. G. Bawendi, M. L. Steigerwald, and L. E. Brus, Ann. Rev. Phys. Chem. **41**, 477–496 (1990).
[8]Y.-S. Fu, X. W. Du, S. A Kulinich, J.-S. Qiu, W.-J. Qin, R. Li, J. Sun, and J. Liu, J. Am. Chem. Soc. **129**, 16029–16033 (2007).
[9]T. Wang, S. S. Farvid, M. Abulikemu, and P. V. Radovanovic, J. Am. Chem. Soc. **132**, 9250–9252 (2010).
[10]N. S. Norberg and D. R. Gamelin, J. Phys. Chem. B **109**, 20810–20816 (2005).
[11]R. N. Bhargava, D. Gallagher, X. Hong, and A. Nurmikko, Phys. Rev. Lett. **72**, 416–419 (1994).
[12]A. B. Djurisić and Y. H. Leung, Small **2**, 944–961 (2006).
[13]D. F. Crabtree, J. Phys. D: Appl. Phys. **11**, 1543–1551 (1978).
[14]G. Blasse, A. Bril, and W. C. Nieuwpoort, J. Phys. Chem. Solids **27**, 1587–1592 (1966).
[15]M. Nogami, E. Takehiro, and H. Tomokatsu, J. Lum. **97**, 147–152 (2002).
[16]S. Dabboussi, H. Elhouichet, H. Ajlani, A. Moadhen, M. Oueslati, and J. A. Roger, J. Lumin. **121**, 507–516 (2006).
[17]T. Hayakawa and M. Nogami, Sci. Technol. Adv. Mater. **6**, 66–70 (2005).
[18]S.-S. Chang and M. S. Jo, Ceram. Int. **33**, 511–514 (2007).
[19]T. Moon, S.-T. Hwang, D.-R. Jung, D. Son, C. Kim, J. Kim, M. Kang, and B. Park, J. Phys. Chem. C **111**, 4164–4167 (2007).
[20]I. Weber, A. Valentini, L. F. D. Probst, E. Longo, and E. R. Leite, Mater. Lett. **62**, 1677–1680 (2008).
[21]X. Fu, H. Zhang, S. Niu, and Q. Xin, J. Solid State Chem. **178**, 603–607 (2005).
[22]A. Kar and A. Patra, J. Phys. Chem. C **113**, 4375–4380 (2009).
[23]T. Matsuoka, T. Tohda, and T. Nitta, J. Electrochem. Soc. **130**, 417–423 (1983).
[24]S. Bazargan, N. F. Heinig, D. Pradhan, and K. T. Leung, Crystal Growth Des. **11**, 247–255 (2011).
[25]J Szuber, G Czempik, R Larciprete, D Koziej, and B Adamowicz, Thin Solid Films **391**, 198–203 (2001).
[26]J. M. Lawrence, P. S. Riseborough, and R. D. Parks, Rep. Prog. Phys. **44**(1), 1–84 (1981).
[27]C. Laubschat, B. Perscheid, and W. D. Schneider, Phys. Rev. B **28**, 4342–4348 (1983).
[28]W. D. Schneider, C. Laubschat, I. Nowik, and G. Kaindl, Phys. Rev. B **24**, 5422–5425 (1981).
[29]J. F. Moulder, W. F. Stickle, P. E. Sobol, and K. D. Bomben, *Handbook of X-ray Photoelectron Spectroscopy* (Perkin-Elmer Corporation Physical Electronics Division, Eden Prairie, 1992).
[30]M. Dejneka, E. Snitzer, and R. E. Riman, J. Lumin. **65**, 227–245 (1995).
[31]D. Lahiri, R. S. Ningthoujam, D. Bhattacharyya, and S. M. Sharma, J. Appl. Phys. **107**, 054316 (2010).
[32]S. Bazargan, N. F. Heinig, J. F. Rios, and K. T. Leung, J. Phys. Chem. C **116**, 4979–4985 (2012).
[33]J. Chen, J. Wang, F. Zhang, D. Yan, G. Zhang, R. Zhuo, and P. Yan, J. Phys. D: Appl. Phys. **41**, 105306 (2008).
[34]G. Kortum, W. Braun, and G. Herzog, Angew. Chem. **2**, 333–404 (1963).